JOINT EUROPEAN TORUS

JET–P(90)69

F.B. Marcus, J.M. Adams, R. Gill, O.N. Jarvis, G. Sadler, P. Smeulders,
P. van Belle, N. Watkins, R.D. Gill, A. Edwards, D. Pasini, S. Wolfe
and JET Team

Two Papers Presented to IAEA Technical Committee Meeting

Two Papers Presented to IAEA Technical Committee Meeting

F.B. Marcus, J.M. Adams[1] R. Gill, O.N. Jarvis, G. Sadler, P. Smeulders, P. van Belle, N. Watkins[1], R.D. Gill, A. Edwards, D. Pasini, S. Wolfe and JET Team*

JET-Joint Undertaking, Culham Science Centre, OX14 3DB, Abingdon, UK

[1]AEA Industrial Technology, Harwell Laboratory, Didcot, OXll ORA, UK
** See Appendix 1*

Preprint of Paper to be submitted for publication in
IAEA Technical Committee Proceedings

TOMOGRAPHIC ANALYSIS OF DATA FROM THE JET NEUTRON PROFILE MONITOR TO DEDUCE THE 2-D SPATIAL AND TEMPORAL EVOLUTION OF NEUTRON EMISSIVITY

F B Marcus, J M Adams[1], R Gill, O N Jarvis, G Sadler, P Smeulders, P van Belle and N Watkins[1]

JET Joint Undertaking, Abingdon, Oxon OX14 3EA, UK
[1] AEA Industrial Technology, Harwell Laboratory, Didcot, OX11 0RA, UK

ABSTRACT *Measurements from the JET neutron profile monitor are analyzed tomographically to deduce the two-dimensional spatial distribution of neutron emissivity and its temporal evolution. The most dramatic change in the emissivity profile is produced by a sawtooth crash. The profiles before and after a sawtooth crash are determined and changes in their characteristics, such as width and amplitude, are compared to those deduced from other diagnostics, including soft X-rays, electron density interferometers and electron cyclotron emission. The drop in the central neutron emissivity can be much larger than that obtained from the integrated global neutron emission, and hollow emissivity profiles are produced. The observed inversion radius is the same on neutron, soft X-ray, and electron temperature profiles. This hollow profile can be understood by observations of the soft X-ray emissivity on the fastest time-scale. A major theme of this paper is that much more information and understanding can be gained if several diagnostics are used together, with their different resolutions, time-scales and physical properties measured.*

1. INTRODUCTION

The JET neutron profile monitor [1] consists of two orthogonal cameras which allow a two-dimensional spatial reconstruction of the plasma emissivity as a function of time. In conferences [1-3] and an expanded publication [4], the methods used to analyse the neutron profile monitor data and results on observations of sawtooth crashes are presented. The tomographic method used here, which is fully described in [5], uses near-elliptic contours described by a 4-term Fourier poloidal expansion and radial Abel inversion. The method will be briefly summarized in this paper. This method has been compared with an alternative method in [5] using Zernicke polynomials, and similar results are obtained in the case of soft X-ray analysis using many channels. The main emphasis of this paper is not in the details of the tomographic method. It is rather to demonstrate how a more complete understanding of plasma physics phenomena may be obtained by cross-comparison of 2-D diagnostics using similar analysis techniques, and by further cross-comparisons with 1-D diagnostics in appropriate cross-sectional cuts.

The particular result of neutron emissivity analysis to be considered is the observation that the emissivity is peaked before a sawtooth crash, and hollow afterwards. Since the time and spatial resolutions of the neutron cameras are limited, the before and after states of the neutron emissivity can be understood by watching the evolution of soft X-ray emissivity, which displays much better spatial and temporal resolutions. The soft X-ray results themselves and accompanying models of sawtooth crashes in JET have been summarized elsewhere [6,7] and at this meeting [8]. The information is further supplemented by 1-D electron temperature and density measurements. For completeness,

it can be noted that 2-D electron temperature profiles have been determined using electron cyclotron emission measurements during plasma rotation [6].

2. INSTRUMENTAL DETAILS AND DATA ANALYSIS METHODS

The neutron profile monitor [1] is shown in Fig. 1 with the lines-of-sight delineated. It consists of 2 high density concrete (3400 kg m^{-3}) fan-shaped multi-collimator cameras with 10 horizontal channels and 9 vertical channels and NE-213 scintillators to detect 2.45 MeV neutrons. The scintillators are operated with pulse shape discrimination of neutrons and gamma rays, and a lower energy detection bias of 2 MeV to reject scattered neutrons.

The raw data are corrected for neutrons back-scattered from material in the lines-of-sight, detector live time, detection efficiency, neutron attenuation, collimator scattering and collimator solid angles. One channel (#11) is rejected due to excessive gamma ray counts.

For the examples given here, the viewing width in the poloidal plane is 0.1 m in the central channels, widening to 0.2 m in the edge channels. The channel separation is 0.2 m in the central plasma region. The channel-to-channel efficiency has a systematic error of about 10%. To obtain a statistical error of less than 10% requires a global emission of 10^{16}n s^{-1} for 10ms, or correspondingly longer times at lower emission rates to achieve sufficient counts in the channels viewing significant neutron emission.

Neutron emissivity profiles in 1-D have previously been unfolded from profile monitor measurements using the program "ORION" [9]. "ORION" uses flux surfaces from an MHD equilibrium and assumes them to be surfaces of constant neutron emission. A best fitting curve is generated by an analytical source function with a small number of free parameters. The plasma neutron emissivity has also been calculated a priori in the 2-D plasma transport code "TRANSP", as discussed in [10]. The result is integrated along the profile monitor's lines-of-sight and agrees acceptably with the experimental data.

In this paper, constrained tomography as discussed in [5] is used to determine the 2-D neutron emissivity profile from the line-integral measurements. A standard geometry is chosen for the inversion using nested elliptical surfaces with fixed ellipticity and centre chosen from MHD equilibrium analysis, with a maximum horizontal minor radius of 1.0 m. Because the deduced emissivity can vary strongly along a poloidal surface, the deduced shape of the emissivity profile can be completely different from the solution geometry, and is relatively independent of the choice of axis and ellipticity of this geometry. The profile can have a different centre than the standard geometry and varying elongation and shape. Near-elliptic contours described by a 4-term Fourier expansion poloidally and radial Abel inversion are employed for the tomographic analysis. The lines-of-sight are assumed to be of zero width in the analysis program, which is a good approximation for profiles with weak gradients. The analysis program initially smoothes the measured channel data into synthesized 100-channel signals for each camera before the inversions are performed, to avoid unphysical oscillations exceeding the camera resolution in the tomographic solution. Further smoothing is performed during the tomographic inversion. The amount of smoothing is chosen so that the deduced emissivity profile gives line-integrals which are within one standard deviation (10%) of the original experimental measurements.

Given these limitations, the amount of fine structure detail obtainable is rather limited. Tests using model profiles generated by the "ORION" code and including 10% random errors show that peaked, flat, hollow, double humped, and outwardly shifted

profiles, when reconstructed by 2-D tomography, can be distinguished from each other. The correct emissivity values can be calculated. The advantages of 2-D tomography not restricted by geometry are that emissivity profiles may be found which were not guessed a priori, and that departures from constant emission on a flux surface may be observed.

3. RESULTS OF NEUTRON TOMOGRAPHY

In the sawtooth crashes in JET discharges 20981 and 20983 discussed in [3,4], fast soft X-ray data are not available at the time slices considered. Recently, an improved soft X-ray triggering system has made fast (200 kHz) data more available [11], along with electron temperature (Te) data, typically at several kHz. To obtain the best time resolution on the neutron profile monitor, a high emissivity is required. Since neutron emissivity at a high level is often dominated by beam-plasma reactions between neutral beam injected deuterium and thermal deuterium, the time-scale must be about 10^{-2}s, an order of magnitude less than typical beam slowing down times. A sawtooth crash redistribution of the neutron emissivity at high emission rates is therefore an indication of the redistribution of neutral beam injected fast ions, in regimes where the thermal deuteron density is relatively flat, and thermal deuteron fusion rates are relatively small.

As a particular example, we consider JET discharge 22202, which has a high neutron yield. It is a 4.7 MA deuterium plasma in a double-null configuration limited on the inner wall, in the H-mode. The plasma is heated with 9 MW of deuterium beams at 80 and 140 keV at the time of the sawtooth crash. We examine the sawtooth crash occurring at 13.412 s after discharge initiation.

First, we examine the neutron emissivity profile before (13.395-13.405 s) and after (13.415-13.425 s) the sawtooth crash which occurs at 13.412 s. The tomographic reconstructions are shown in Fig. 2 with the emissivity versus radius at the midplane in a 1-D cut, and in Figs. 3a and 3b, with a display of the 2-D neutron emissivity in major radius and height, before and after the sawtooth crash. The neutron emissivity before the crash is peaked at about major radius R = 3.05-3.15 m, with a maximum emissivity of $4\times10^{14}m^{-3}s^{-1}$, and a Full Width Half Maximum (FWHM) of 0.60 m. The FWHM is taken on the emissivity along a chord in major radius through the midplane, and does not involve a poloidal average. After the crash, the emissivity profile is hollow, with a new maximum emissivity (off-centre) of $1.3\times10^{14}m^{-3}s^{-1}$. The axial emissivity is about 40% of the off-centre maximum. For the hollow profile, defining the FWHM to be the full width of the region on the mid-plane where the emissivity outside the maximum is half the maximum, the FWHM is 1.3 m. Comparing the before and after emissivities along the radial chord, the inversion points, or equal emissivities, occur at R=2.60 m and 3.45 m.

An examination of the accuracy of the tomographic reconstruction illustrates several aspects of the method chosen. When the emissivity is integrated over the entire emitting volume, the global emission is about 10% higher than the values measured by calibrated fission chambers, well within the combined error for both systems [4]. Again using the reconstructed neutron emissivity, line integrals of emission are calculated and compared to the original experimental measurements. Due to the analysis method, the calculated and experimental line-integrals agree to within 5% for channels intersecting the outer (in minor radius) regions of the plasma. The differences are always largest for channels intersecting the inner region, reaching up to 10%, which is still within experimental accuracy. This occurs because this tomographic inversion method near the plasma centre depends on the emissivity calculated in the outer plasma regions, whereas emissivity in the outer regions depends only on outer region measurements. Furthermore, small errors

in the reconstruction are only obtained when the measurements from the horizontal camera and vertical camera measurements of the same region are self-consistent. (We note at this point that the errors in the central, as well as the outer, region can be made much smaller by multiplying the vertical camera by a constant (~0.95), but there is no justification for doing this, since all geometry has been considered as accurately as possible for both cameras.) In the reconstruction, all channels, except vertical channels #11 and #15, give reconstructed line integrals within 10%. Channel #11 was eliminated due to a known experimental problem, an excessive gamma count, which is measured by the pulse shape discriminator. In the case of channel #15, the central vertical channel, the experimental value is 35% higher than the reconstructed values, both before and after the sawtooth crash. To investigate this, a 1-D unfolding method using the ORION code is used with predetermined profiles, and a chi-squared minimisation is used. Again, channel #15 had by far the largest error, even though it was weighted most heavily in the fitting method. Channel #15 is therefore considered anomalous, and a subsequent investigation is indicating that, at this time, #15 had an unreasonably high neutron energy threshold, for which the efficiency was over-compensated. For discharges taken on different days, channel #15 is consistent with other channels. The inferences are that: a) details of tomographic unfolding by this method [5] are least accurate on axis; b) the method provides a means of identifying channels which may have a correctable hardware fault. With all these caveats, the emissivity profile is still very hollow after the crash, and we want to understand how this happens.

4. ELECTRON DENSITY AND TEMPERATURE 1-D PROFILES

The line-average electron density is measured with 6 vertical interferometer channels, at major radii of 1.89, 2.17, 2.70, 3.02, 3.35, and 3.75 m, in this case with a 25 Hz sampling rate. As a result of the sawtooth crash, only the central channel shows a noticeable change, dropping by 29%. The limited spatial resolution makes it difficult to determine the exact nature of the density profile change. To analyse the profile, a method is used [12] in which a function of MHD flux surface, allowing peaked, locally flat, or hollow profiles, is obtained by a least squares fit to the line of sight integrals. The axial density obtained by this method changes from $2.8 \times 10^{19} m^{-3}$ to $1.4 \times 10^{19} m^{-3}$ as a result of the sawtooth crash, while the volume averaged density drops by only 1/10 from $1.3 \times 10^{19} m^{-3}$. The profile shape changes from peaked to slightly hollow, where the axial value after the crash is 3/4 of the maximum value of the density off-axis. A similar profile is found by Abel inversion. With only six channels, density profile accuracy, especially for hollow profiles, is limited. If the thermal deuteron density is proportional to the electron density, the change in the density profile provides part of the explanation for the change in neutron emissivity profile, although the neutron emissivity profile is much more hollow. Since the electron density is the sum of electrons provided by the thermal deuteron density, the fast ion density, and the impurities, it is difficult to draw a firm conclusion. For example, part of the hollowness of the electron density profile could be due to a hollowness in the fast ion profile. Also, the electron density profile in the next time sample becomes flat in the central regions, indicating that the density profile is evolving on the time-scale of the sampling.

Next we examine 1-D profile electron temperature data from the electron cyclotron emission grating polychromater, here operating at 3 kHz (a much faster rate than the density) and measured at the plasma midplane as a function of major radius. The electron temperature versus time is shown in Fig. 4, for 8 of the 12 channels, going from the

innermost channel at R=3.25m out to 3.78m. On this time-scale, the electron temperature profile becomes nearly flat at 4.1 to 4.4 keV at major radii out to 3.63m, with a slight hollowness of about 10%, and with a profile inversion occurring at R=3.5m. This picture is supported on a 30Hz sampling rate by data from the electron cyclotron emission Michelson interferometer. The inversion radius is approximately the same as for the neutrons. There is no indication as to how the neutron emissivity becomes strongly hollow.

5. RESULTS OF SOFT X-RAY (SXR) TOMOGRAPHY

We examine the SXR emission data from a vertical camera with 38 channels and a horizontal camera with 62 channels. (This camera is also discussed in detail at this meeting [8].) The tomographic method used in this paper is the same as for the neutrons, and has been shown [5] to give similar results to alternative methods. The SXR camera allows much better spatial and temporal resolutions than the neutron camera, with more channels and up to 200 kHz sampling rates. Even with the improved resolution, the reconstructed emissivity gives line integrals that differ by less than 1% of the measured values on the outer channels, but up to 10% on the inner channels, much larger than the measured accuracy. If all the measured emission values of the vertical camera channels are multiplied by 1.04 and the horizontal channels divided by 1.04, then all reconstructed line integrals are within 1-2% of the measurements.

In what follows, all the results have been calculated using a multiplier of 1.04, and the same results as without a multiplier are found for topology and horizontal inversion radius, although the absolute emissivity values differ by 10%. When the profile is peaked on axis, the 1.04 multiplier gives the elongation of the axial emissivity as 1.45, nearly equal to the MHD equilibrium value of 1.35. Otherwise, the result is 1.95, which seems too large. The 1.04 factor has been used on all JET SXR analysis, and is justified by the observation that the multiplier gives the same integrated brightness from both cameras, and is presumed to to compensate for inaccuracies in camera geometry.

To compare with the electron temperature data, we first examine the SXR data at a 10 kHz sampling rate, with data summed over 100 μs intervals. A cross section through the midplane of the deduced SXR emissivity profile is shown in Fig. 5a, for 12 emissivity profiles from 13.411999 s to 13.413098 s, in 100μs steps, plotted versus major radius. The profile is highly peaked before the sawtooth crash, and collapses and broadens to a flat profile after it. The inversion major radii are R=2.65 m and 3.50 m, similar to the neutron and electron temperature data. We note that this similarity was reported for unprocessed line-integral data in [2].

An understanding of the neutron emissivity after the crash is obtained only by looking at the SXR data on the fastest time-scale of 200 kHz, as shown in Fig. 5b, looking at 12 SXR emissivity profiles from 13.412399 s to 13.412510 s, spaced 10μs apart, with a 5μs data summation time. The emissivity profiles at the midplane are shown versus major radius. An examination of Fig. 5 and of level contour plots shows that the maximum in emissivity is observed to move from the axis to off-axis, then rotate and spread out poloidally at an intermediate minor radius. This behaviour has been previously reported, and also seen on electron temperature data using rotation for 2-D reconstruction [6]. The full width of this rotating region at the midplane is about 1 m, similar to the after-crash profile observed on the neutrons.

We therefore conclude that the change in the neutron emissivity is consistent with a model in which the fast ions on axis, which cause most of the neutron emission by

interaction with thermal deuterons, move off-axis with the plasma during a sawtooth crash. The fast ions then spread around a surface poloidally, and stay there while slowing down, causing the observed neutron emissivity profile, which is hollow, and which persists for the beam slowing down time-scale, about 10^{-1}s. The electron temperature and SXR profiles, in contrast, have diffused and become flat on the 1ms time-scale. The electron density profile becomes slightly hollow, and cannot by itself explain the much more hollow neutron emissivity.

6. CONCLUSIONS

We have shown that a combination of several diagnostics with several data sampling rates and spatial resolution can be combined to allow a much improved understanding and cross verification of data. The example shown of a sawtooth crash provides further understanding of how the fast ions redistribute as a result of the crash.

REFERENCES

[1] ADAMS, J.M., CHEETHAM, A., CONROY, et al, Proc. 16th Europ. Conf. Venice, Italy, 1989, **13B** I, 63.

[2] SADLER, G, CONROY, S, JARVIS, O N, VAN BELLE, P, ADAMS, J M, HONE, M, JET Report JET-P(89)77, Presented at IAEA Technical Committee on Alpha-particle Heating, Kiev, USSR, 1989.

[3] MARCUS, F B, ADAMS, J M, CHEETHAM, A, et al, Proc. 17th Europ. Conf., Amsterdam, Netherlands, 1990, Vol. 1, EPS (1990), 331.

[4] MARCUS, F B, ADAMS, J M, CHEETHAM, A, et al, submitted to Plasma Physics and Controlled Fusion

[5] GRANETZ, R.S. and SMEULDERS, P. Nucl. Fusion 28, (1988), 457.

[6] CAMPBELL, D.J., CORDEY, J.G., EDWARDS, A.W., et al, Plasma Phys. and Contr. Nucl. Fus. Res. (Proc. 12th Int. Conf. Nice, France), Vol. 1, (1988), 377.

[7] CAMPBELL, D J, and the JET Team, to be published in Plasma Phys. and Contr. Nucl. Fus. Res. (Proc. 13th Int. Conf. Washington, USA), (1990)

[8] GILL, R, EDWARDS, A W, PASINI, D, and WOLFE, S, Proc. of IAEA Technical Committee Meeting on Time Resolved 2-D and 3-D Plasma Diagnostics, Nagoya, Japan, (1990).

[9] CONROY, S.W. (1990) Diagnosis of Fusion Products for Reactor Relevant Plasmas, Ph.D. Thesis, Imperial College, London, UK. (1990)

[10] SADLER, G. et al, JET Report JET-P(90)10, (1990) Submitted to Nucl. Fusion.

[11] EDWARDS, A, Proc. of 8th Topical Conf. on High Temp. Diag., Hyannis, USA, (1990).

[12] SMEULDERS, P, KARDAUN, O, CHRISTIANSEN, J P, ELLIS, J, GOTTARDI, N, JET Report JET-R(89)09, (1989)

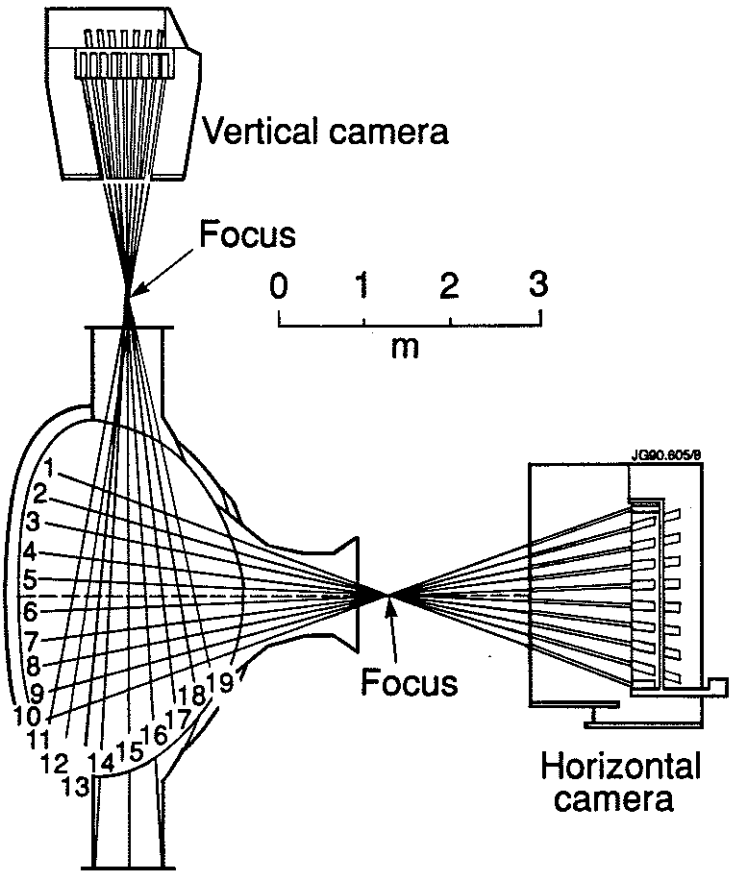

Fig.1. JET neutron profile monitor

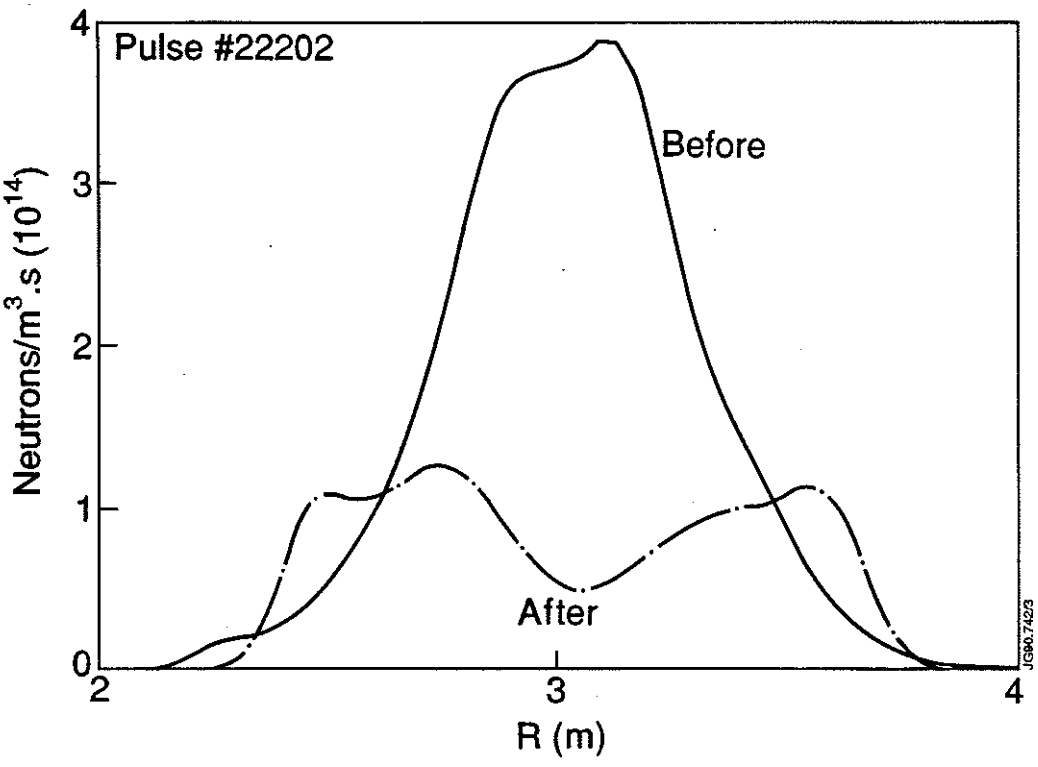

Fig.2. Pulse #22202 - neutron emissivity versus major radius before (13.395 - 13.405 s) and after (13.415 - 13.425 s) a sawtooth crash

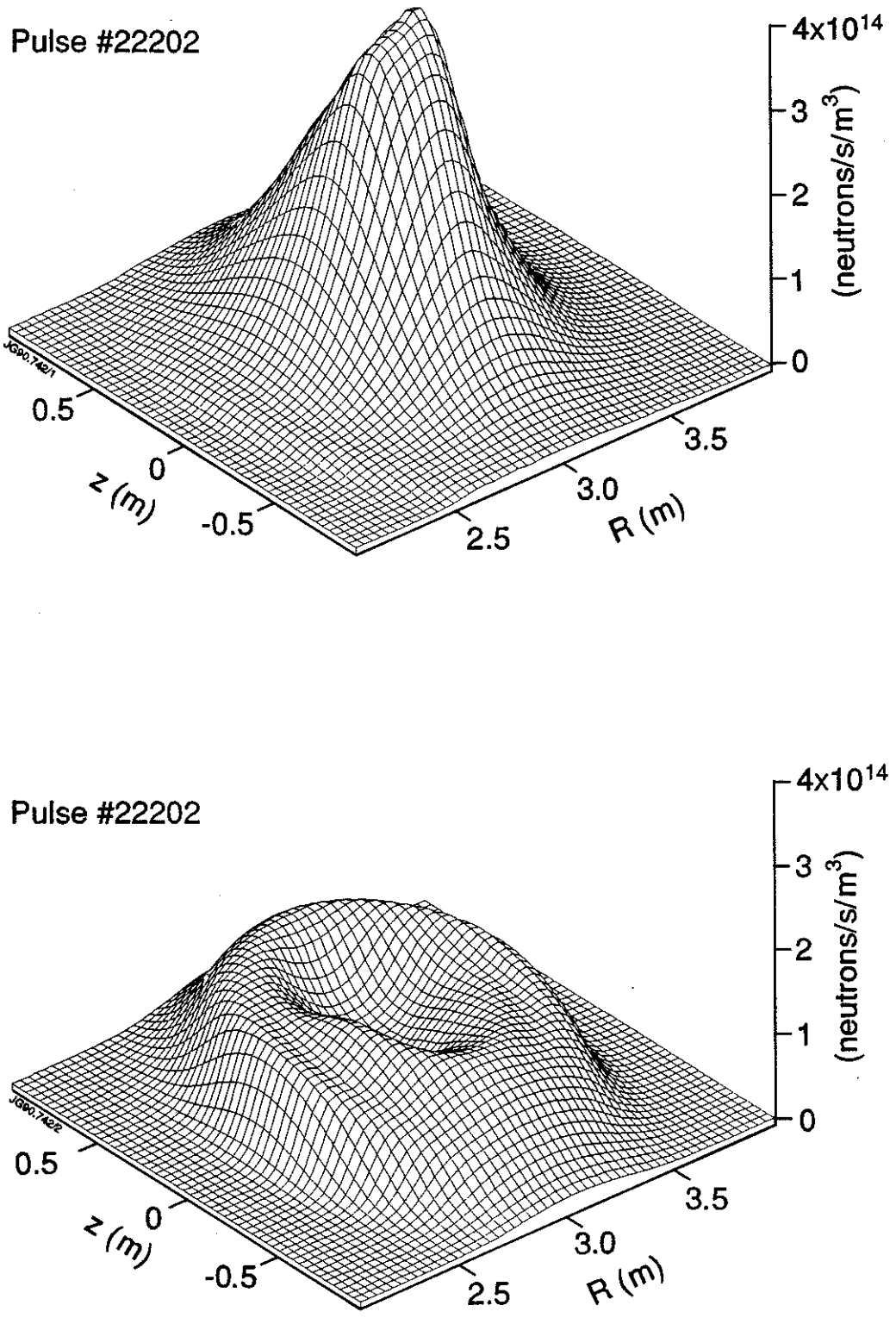

Fig.3. Pulse #22202 - neutron emissivity versus major radius and height:
a) before (13.395 - 13.405 s); and b) after (13.415 - 13.425 s) a sawtooth crash

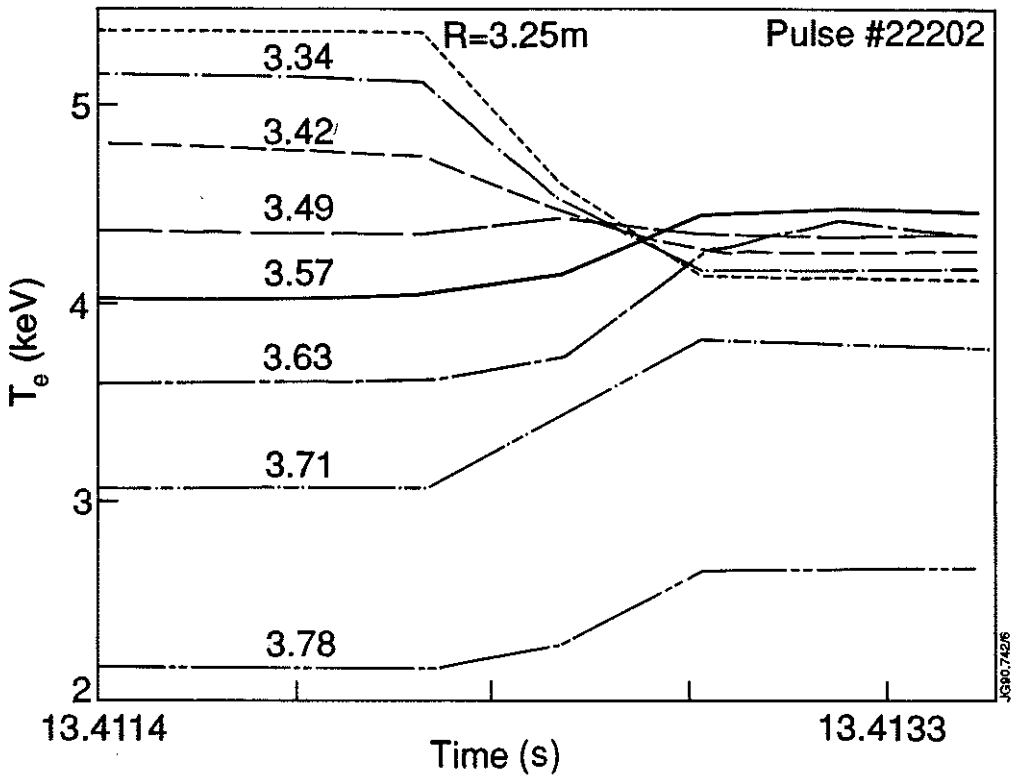

Fig.4. Pulse #22202 - electron temperature versus time for several major radii

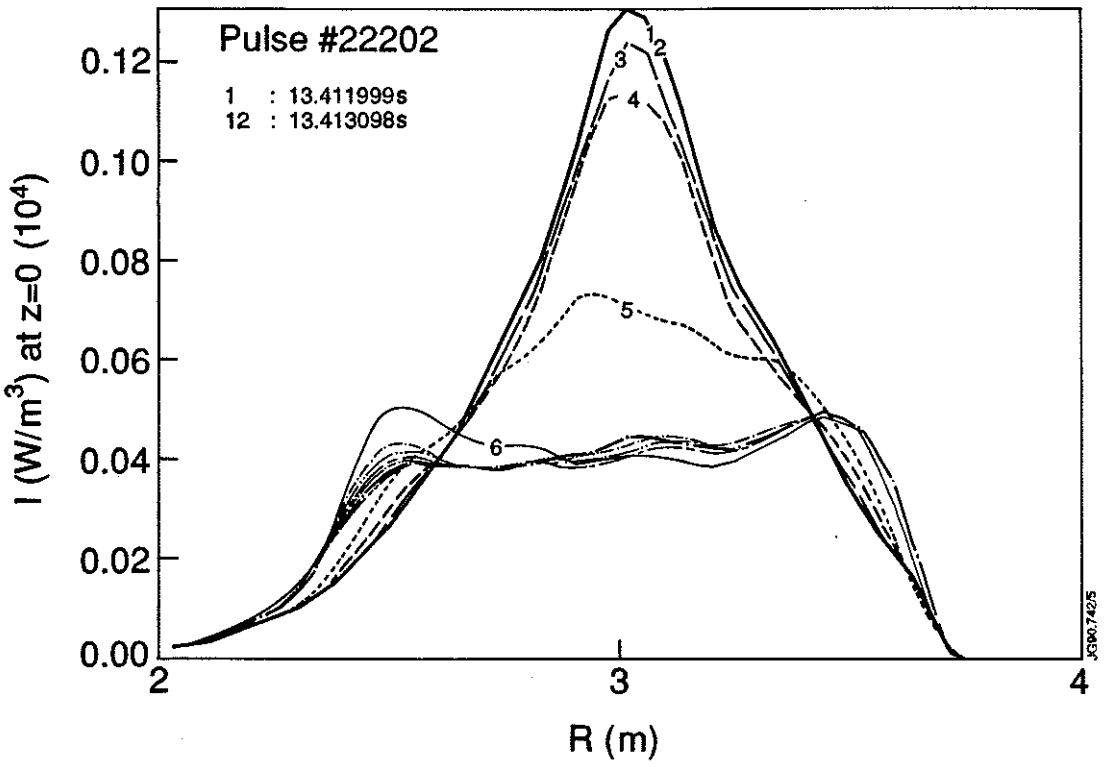

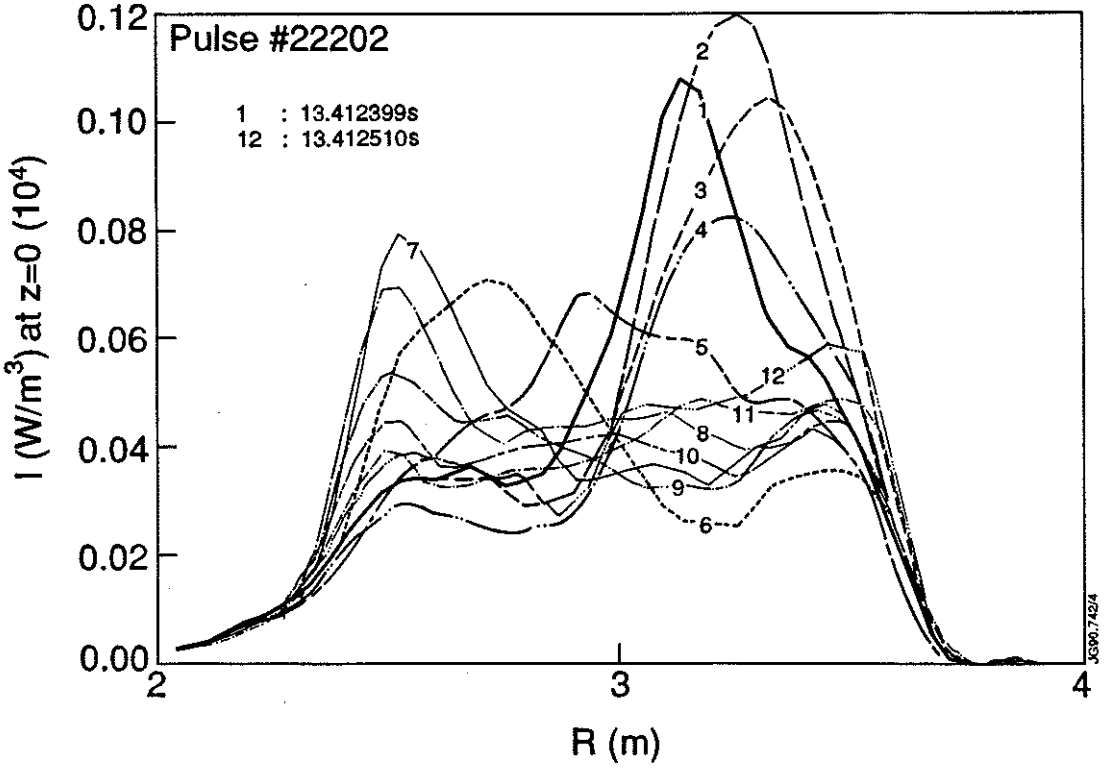

Fig.5. Pulse #22202 - SXR emissivity versus major radius for twelve equally spaced times: a) 10 kHz; and b) 200 kHz

DETERMINATION OF TOKAMAK PLASMA BEHAVIOUR AND PARAMETERS FROM TOMOGRAPHIC ANALYSIS OF SOFT X-RAY CAMERA DATA

R D Gill, A Edwards, D Pasini, and S Wolfe

JET Joint Undertaking, Abingdon, Oxon., OX14 3EA, UK

Equipment Two soft X-ray cameras and a set of toroidal detectors view the JET plasma. The cameras[1] view the plasma from both vertical and horizontal directions (fig. 1) in the same plane and contain 38 detectors mounted in a single row and 62 detectors in three parallel rows respectively. The diffused Si detectors are shielded by Be or Aℓ foil and the signals are digitised at up to 200 kHz. The relative response of each detector was calibrated to 0.5% with a radio-active source and spurious electrical noise was virtually absent due to a carefully designed earthing system. Five toroidal detectors assemblies have been installed, each containing 4 individual detectors viewing the region of m=1 activity. An attempt was made to install these at optimum toroidal angles $\varphi = \pi/n$ (fig. 2), but this was not entirely possible due to port availability.

Data acquisition and processing. Data from the 120 channels can be stored in 1k blocks at 200, 10, 1 or 0.1 kHz. Because of data storage restrictions (~3.5 MW) data in the higher frequency blocks has to be selected by either a software or hardware trigger. A new hardware trigger system has just been installed which operates by using a preprogrammed micro-processor[2] to look in real time for events of interest on any 4 channels. This has been particularly successful in trapping mhd oscillations and partial sawteeth as well as disruptions, pellets and normal or monster sawteeth. After a pulse the data is filed in a central store and can be accessed and displayed by a suite of programmes.

Tomography

The observed soft X-ray signals are integrals along a line of sight $I = \Omega \int \epsilon(x)\, \alpha(E_x)\, dx\, dE_x$ where Ω is the solid angle, $\epsilon(x)$ the plasma emissivity and $\alpha(E_x)$ the transmission coefficient of the X-ray filter. For many purposes the spatially resolved emissivity $G(r, \theta)$ is required and is obtained by a tomographic

inversion of the raw data[3]. Most work in JET has used the Cormack method based on an expansion in Zernicke polynomials, $R_{\ell m}$,

$$G(r\theta)=\sum_{\ell m} (A^s_{m\ell} \sin\ m\theta + A^c_{m\ell} \cos m\theta) R_{\ell m}(r)$$

to describe the inverted data and the expansion

$$F(p,\chi)=\sum_{\ell m} (A^s_{m\ell} \sin\ m\chi + A^c_{m\ell} \cos m\chi) S_{\ell m}(p)$$

to describe the line integral data with $S_{\ell m}(p) = 2 \sin [(m + 2\ell + 1) \cos^{-1} p]/(m + 2\ell + 1)$ and χ the detector angle. The coefficients $A^{s,c}_{m\ell}$ are then determined by a fit to the experimental data. The maximum values of ℓ and m which can be used depend on the experimental assembly with ℓ determined by the radial resolution to a maximum of about 12 on JET. m is determined from the maximum number of independent views of a particular surface of constant p. In JET the two cameras provide essentially four independent views and thus one can determine a maximum of 4 coefficients $A^{s,c}_{m\ell}$ which are typically A_{oo}, $A^{s,c}_{1\ell}$, $A^c_{2\ell}$. Higher m-number modes will alias down to appear as combinations of lower m-modes.

Using high speed data processing based on transputers, it is possible[4] to carry out the tomographic inversion in real time and provide a simultaneous display of the data on a colour monitor at a rate of $\geq$ 25 fps. The JET system uses a network of INMOS transputers and has just been successfully commissioned.

Applications The JET X-ray cameras have made major contributions to the understanding of sawteeth, disruptions, pellet injection, the snake, radiation profiles and impurity diffusion and mhd efforts generally.

Sawteeth Sawteeth in JET have been studied extensively with tomographic analysis of the fast crash phase. Generally, JET sawteeth have neither successor nor precursor oscillations and this considerably simplifies the analysis. However, the new trigger system has the flexibility to select sawteeth associated with mhd oscillations and as a result many examples of partial sawteeth and sawteeth with mhd oscillations have been found.

Initial work[5] on JET centred around the analysis of both normal and monster sawteeth with no mhd oscillations. Monster sawteeth, for example, have a long duration (several s) and have a very large amplitude of crash which occurs on a

rapid timescale (≤ 100 μsec) but well within the instrumental time resolution. The tomographic reconstructions of the sawtooth in fig. 3 show (fig. 4) that the crash occurs as a displacement of the hot central core off axis to form a crescent shape which then decays. All JET sawteeth correspond to this pattern. It has been suggested that the observed patterns can be described by a convective flow associated with low shear [6].

This interpretation of our data has recently been questioned by various groups (e.g. ref. 7) who have analysed their own data and found it to be described by a Kadomtsev type of model. In order to investigate the validity of our analysis, a simulation has been made[8] of both models from which the X-ray signals have been calculated. These have been input to the tomography code and a comparison of the reconstructions with the original data (fig. 5) shows that our analysis method can very clearly distinguish between the two models at least when the displaced core moves in the median plane. When the core moves at 45° to the median plane ambiguities can arise. This analysis confirms our view that JET sawteeth follow a convective flow pattern.

Sawteeth with successors often occur and tomographic analysis has shown that the rapid part of the collapse still looks convective, but the crescent shaped plasma does not collapse and rotates to produce the observed mhd oscillations.

The more recent data on sawteeth with precursors is only now being analysed. However, preliminary indications are that the precursor phase looks very similar to the initial phases of the fast collapse but developing on a slower timescale. The detail mechanisms of the fast collapse have not yet been understood due to the difficulty of disentangling rotation effects from movements in the plasma core. (fig. 6)

JET sawtooth crash data has also been analysed[9] by the maximum entropy method and this shows general agreement with the Cormack method. However, this method, as applied to JET data, has not yet reached the stage of providing useful noise free reconstructions which are in reasonable agreement with physical expectations, i.e. the outer soft X-ray emission contours often show very poor agreement with the flux surface derived from the magnetic measurements.

Pellets and Snakes

JET is refuelled by injection of solid D_2 pellets with diameters up to 6 mm. The injector is in the median plane with its line of sight in the plane of view of the vertical soft X-ray camera. This has enabled us to make detailed measurements on the plasma-pellet interaction zone and determine from the time trajectory of the pellet its velocity and range (fig. 7). These measurements have been then compared with the results of various calculations. In addition it has been shown that the X-ray emissivity of the pellets is in reasonable agreement with model calculations although the radius of the emitting cloud is somewhat larger than anticipated[10].

Some pellets cross the q=1 magnetic surface and this gives rise to anomalous effects and the plasma-pellet H_α and X-ray emission (fig. 8) decrease severely due to the reduced reservoir of hot electrons which is available at q=1. This effect, which has also been seen on other machines, has been used to calculate[11] that dq/dr is extremely small at q=1.

The most striking effect of the pellets is to produce a small region of high density plasma[12] which persists for seconds, apparently unchanged. The density can be up to twice that of the background plasma, although the temperature is approximately similar. It is thought that this phenomenon ("the snake") is caused by island formation, but convincing explanations of its longevity have not yet appeared. More recently, snakes have been observed (fig. 9) in ohmic discharges at the onset of sawteeth, and generally following an m=1 oscillation. These snakes seem to be dominated by impurities. Tomographic analysis of the snake data would require high poloidal m-numbers to fit the data well and would require the analysis of the data from a complete rotation. This analysis has not yet been carried out but would only be successful for data where the snake rotates uniformly.

Impurity Radiation

The tomographically inverted profile G(rθ) represents the radiated power in the X-ray region transmitted through the filters in front of the detector. This quantity may also be calculated from a knowledge of the plasma density, n_e, temperature, T_e, and impurity concentration,

$$G=\sum_z \int n_e n_z \, S(E,T_e,Z)\, \alpha(E)\, dE$$

assuming coronal equilibrium. S depends on the atomic physics of the impurity. Alternatively, if one impurity makes a predominant contribution to G, then values of n_z may be determined. This technique has been successfully applied to the determination of impurity profiles and diffusion coefficients following laser blow-off experiments[13].

In another series of experiments alternate detectors in the vertical and horizontal cameras have been equipped with different filters. It is then possible to tomographically invert the two profiles separately. The ratios of the emissivities at a particular radius together with a knowledge of the plasma impurity concentration then allow the determination of the plasma temperature and density on a very rapid timescale. This technique is presently being used to study the development of the plasma density and temperature during plasma disruption when other diagnostics often fail. (fig. 10)

Future Developments

It is intended to develop the existing soft X-ray system in JET by (a) increasing the number of detectors in the poloidal plane to improve the poloidal mode number determination, and by (b) designing a new system which can be used in the D-T phase of operations.

(a) Because of port limitations there is no possibility of adding cameras of the sort already described. Instead it has been decided to use an array of diodes mounted on a single chip ~ 4 x 0.5 cms (EG & G PDA-38). These allow the design of extremely compact cameras and the detectors have been successfully used elsewhere particularly at MIT. It is estimated that they will work in the JET neutron radiation environment for up to one year with occasional annealing to reduce the effects of neutron damage. Good signal to noise ratios can be achieved and it is estimated that the neutron induced signals will never be large for D_2 plasmas. A trial of the detectors has already been made with successful results.

The choice of the location of these extra cameras is complicated by the positions of available JET ports and the presence of structures within the torus such as the belt limiter. The aim is to resolve at least up to m=3 and this then implies the addition of at least two full cameras. The positions of these have been guided by the π/m rule but simulations have been made to test the new camera's ability to

reconstruct features with the required m-numbers. It is hoped to install this new system by 1993.

(b) In the D-T phase of operations, neutron and gamma fluxes will increase more than two orders of magnitude and neither the present nor the compact cameras will operate due to the very large radiation damage which will occur. A new system is therefore required. Currently we are pursuing the idea of using a very high mass shield which shields both the neutron and the gammas with good efficiency. This shield could be used with Si detectors but we are also considering the use of other detectors. Such a system would be mechanically decoupled from the machine and would probably have a single view of the plasma from a horizontal port with a reduced number of channels.

References

1. A. W. Edwards et al., Rev. Sci. Instr. 57 (1986) 2142.
2. A. W. Edwards et al., Proc. of 8th Tropical Conference on High Temperature Diagnostics (1990), Hyannis, Mass., USA.
3. R.S. Granetz and P. Smeulders, Nuclear Fusion, 28 (1988) 457.
4. E van der Goot, A.W. Edwards and J Holm, JET-P(89)45.
5. A. W. Edwards et al., Phys. Rev. Lett. 57 (1986) 210.
6. J.A. Wesson, Plasma Physics and Controlled Nuclear Fusion Research 1 (1986) 3 (IAEA, Vienna 1987).
7. C. Janicki, R. Decoste and C. Simm, Phys. Rev. Lett. 62 (1989) 3038
8. S. W. Wolfe, Controlled Fusion and Plasma Heating, 335 (Amsterdam, 1990).
9. L.M. Blush and G.A. Navratil, APS 1981 (Anaheim).
10. R.D. Gill, Nuclear Fusion 29 (1989) 397.
11. R.D. Gill, A.W. Edwards and W. Weller, Nuclear Fusion 29 (1989) 821.
12. A. Weller et al., Phys. Rev. Lett. 59 (1987) 2303.
13. D. Pasini et al., JET-P(90)01.

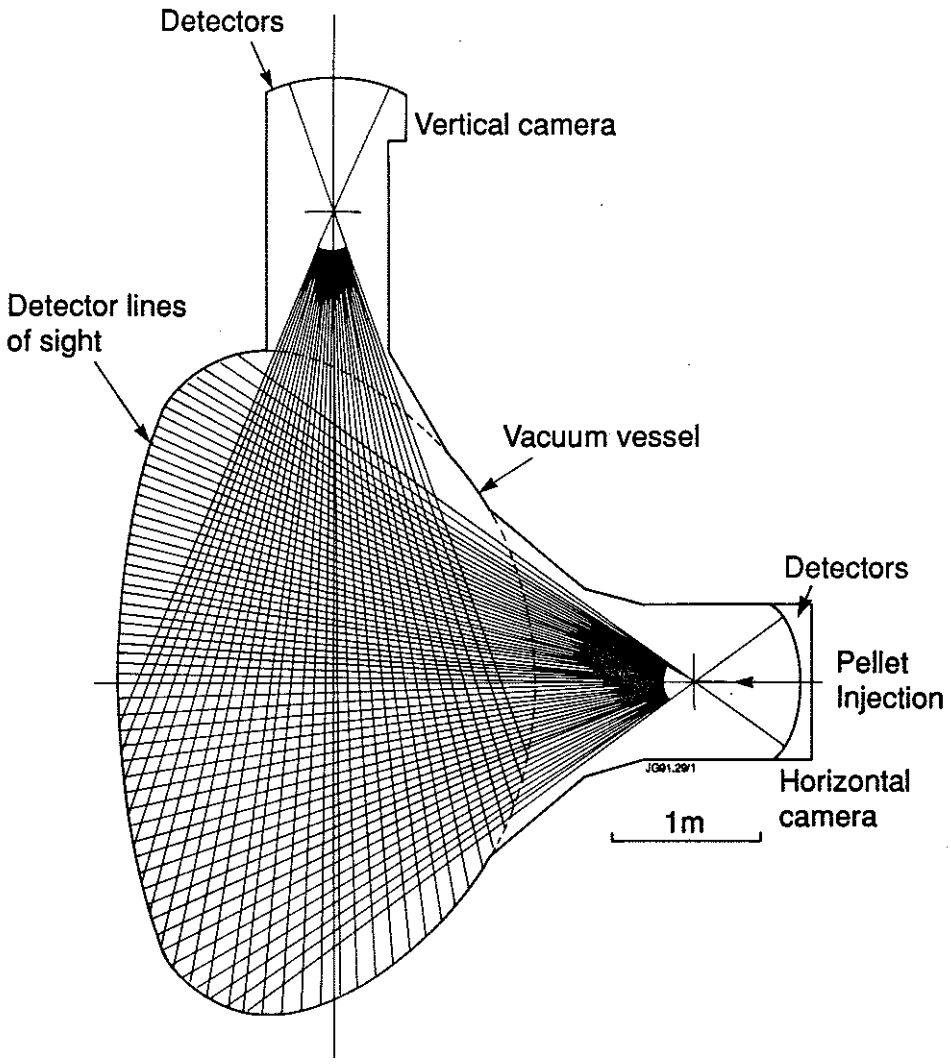

Fig. 1 Location of soft X-ray cameras showing the detector lines of sight.

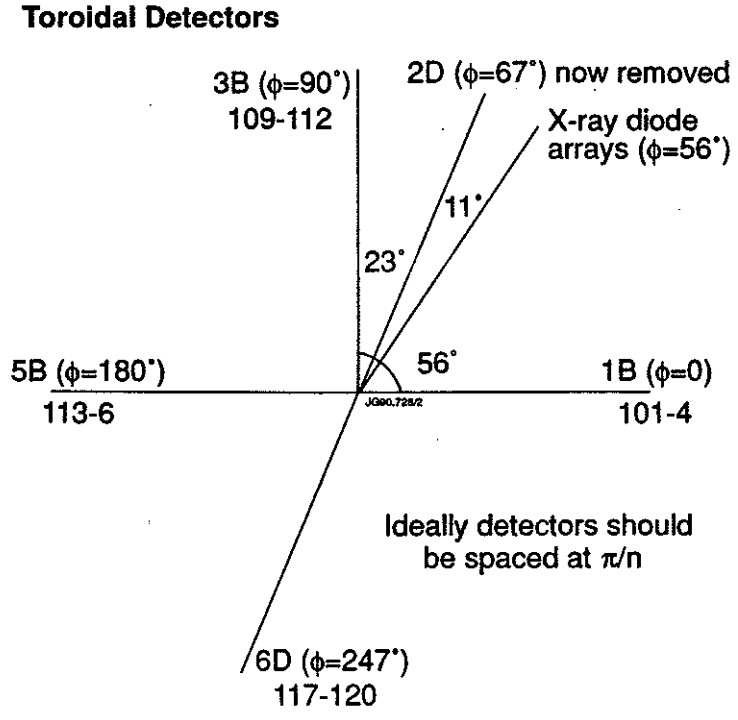

Fig. 2 Positions of the five toroidal cameras.

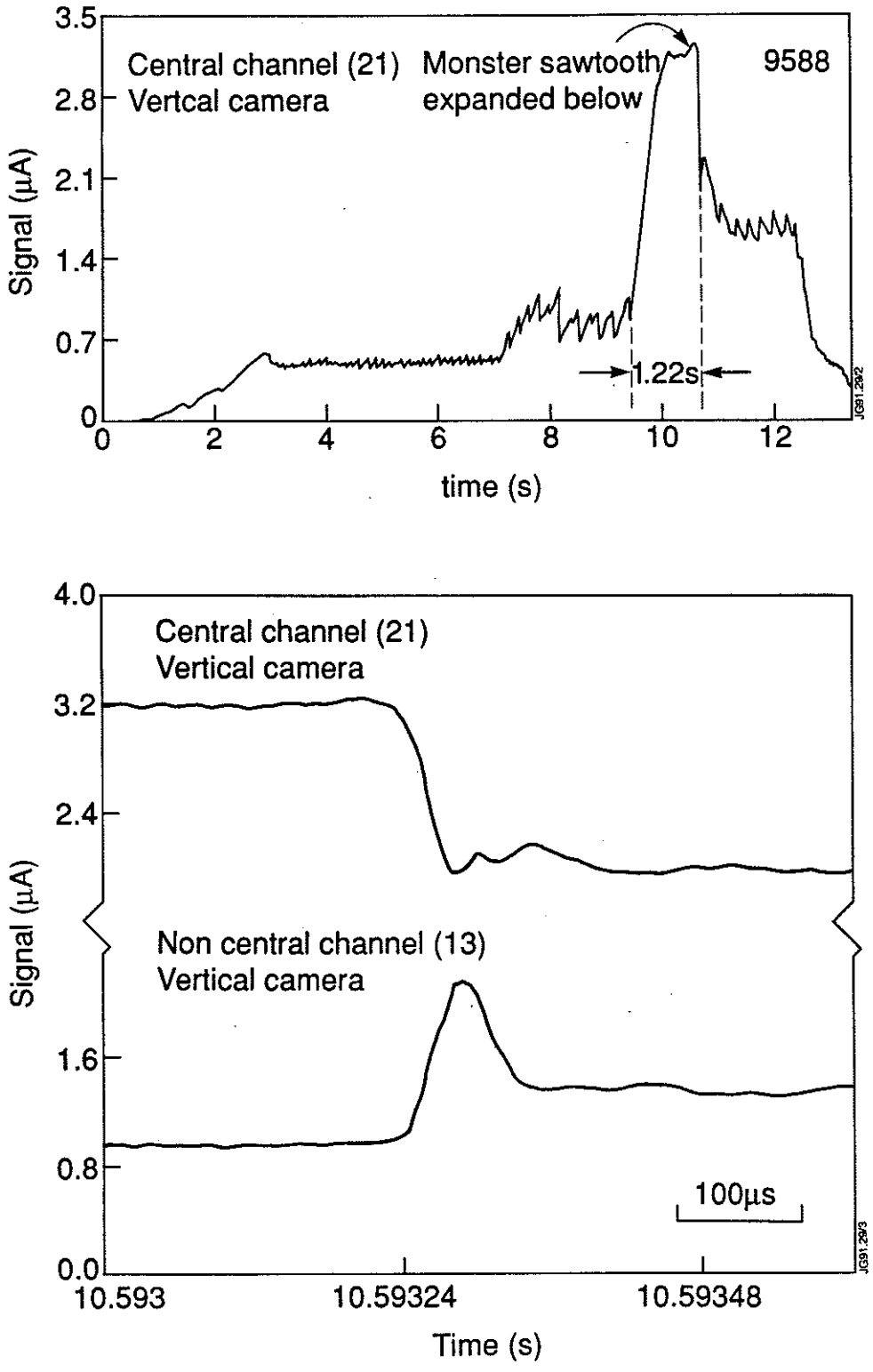

Fig. 3 Sawtooth collapse in an additionally heated discharge.

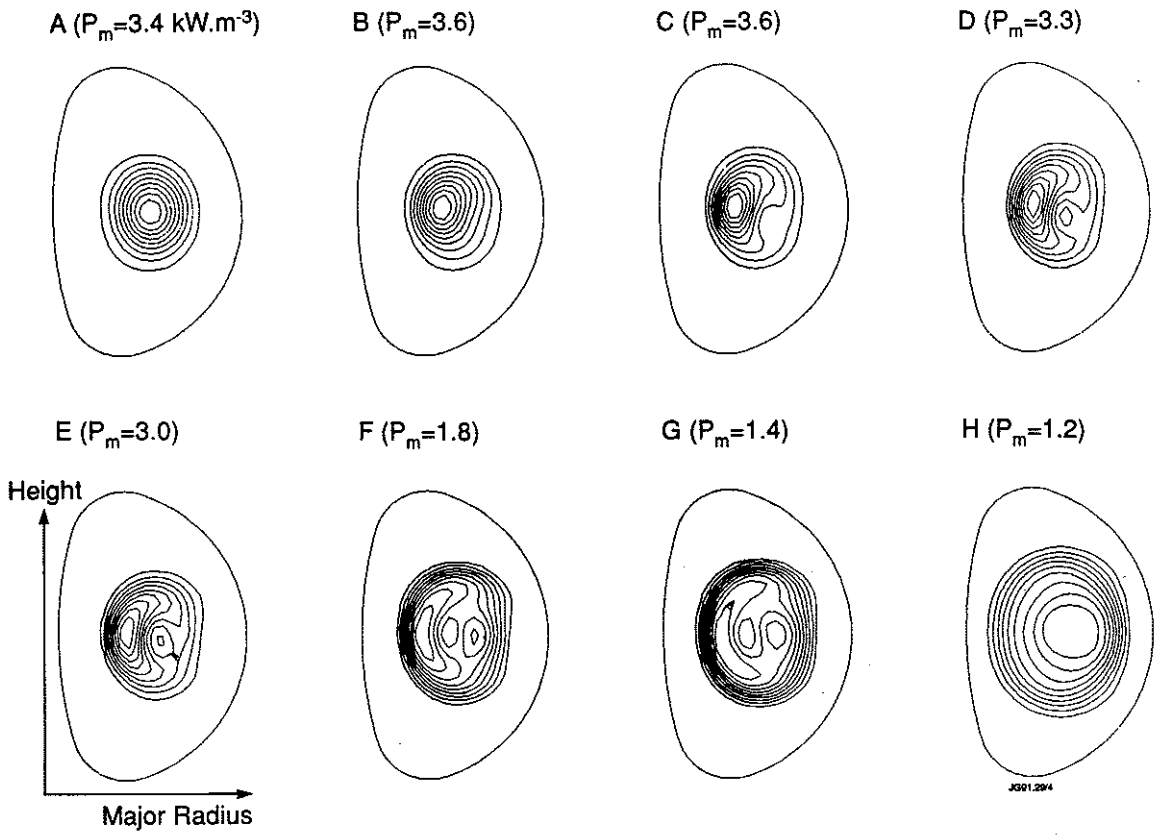

Fig. 4 Tomographic reconstruction of the sawtooth collapse indicated in fig. 3.

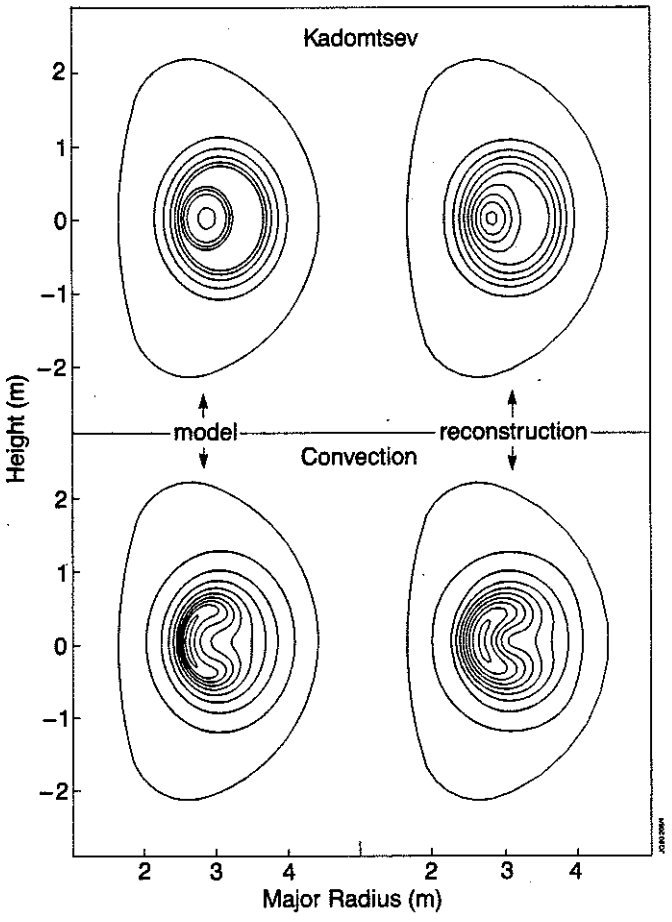

Fig. 5 Comparison between simulated model data and tomographic reconstructions for the Kadomtsev and convection models of the sawtooth collapse.

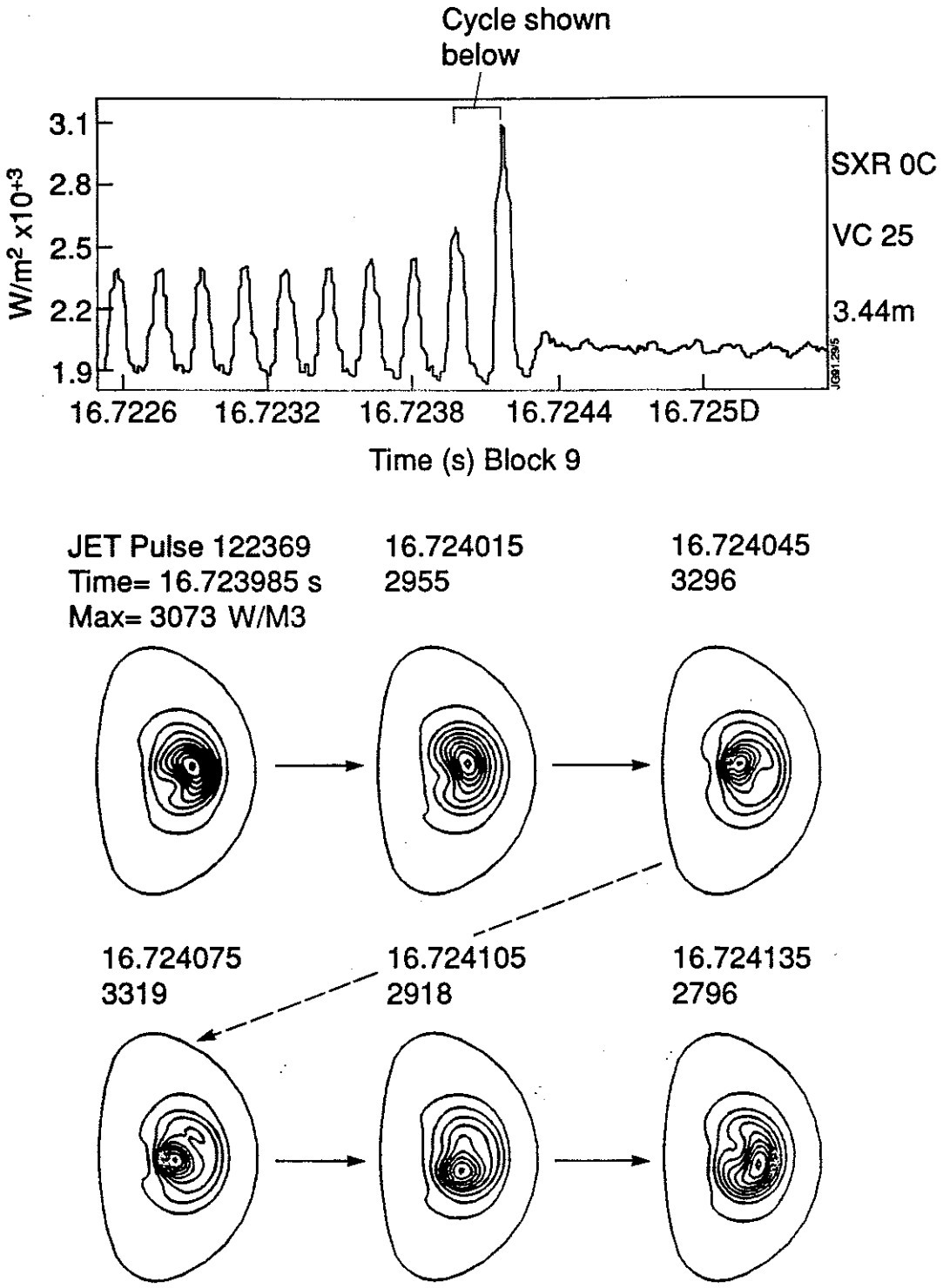

Fig. 6 Tomographic reconstuction of a complete oscillation of a sawtooth precursor.

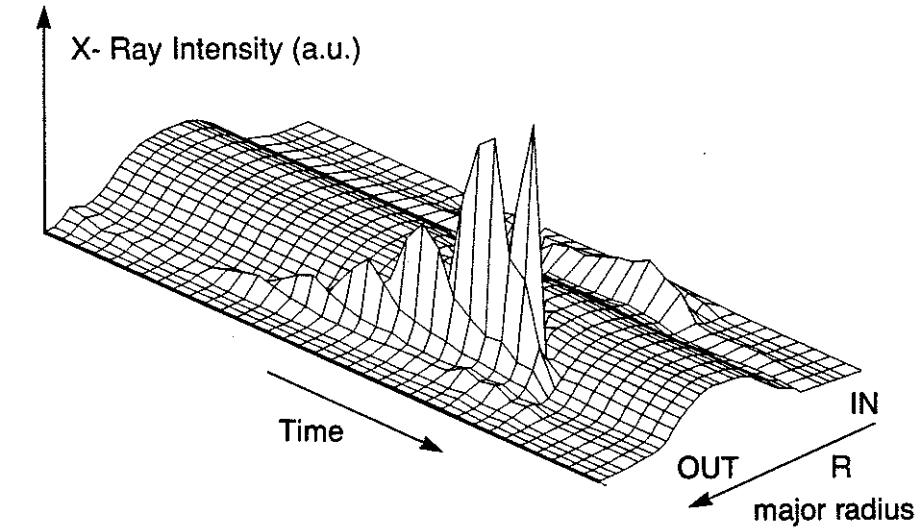

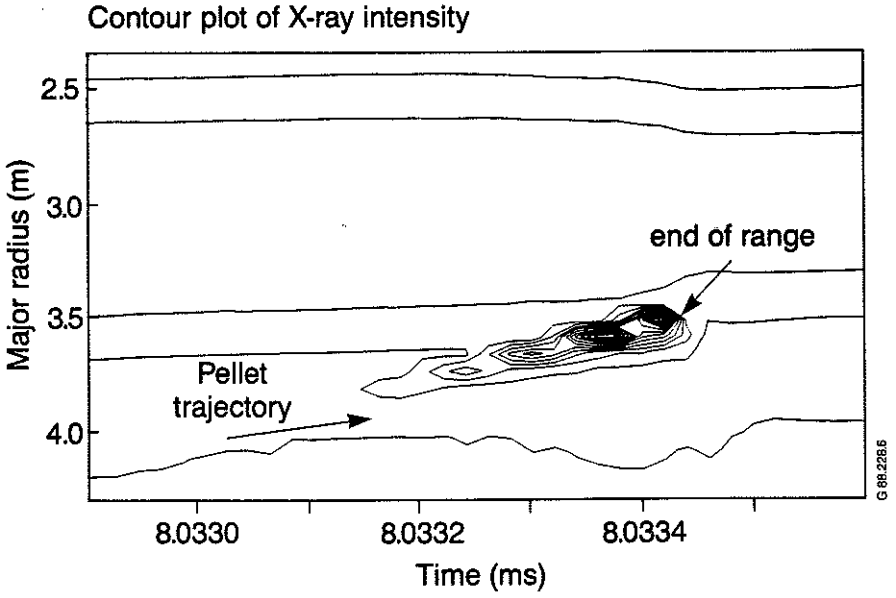

Fig. 7 View of pellet-plasma interaction zone.

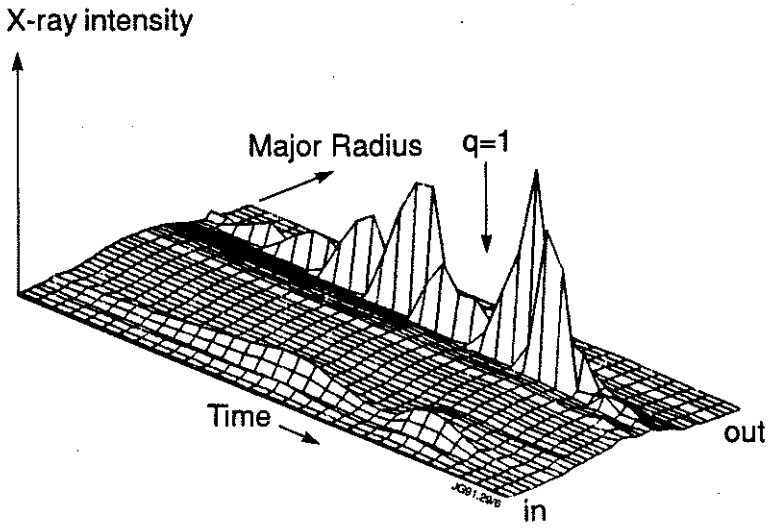

Fig. 8 Dip in X-ray emission as a pellet crosses the q=1 surface.

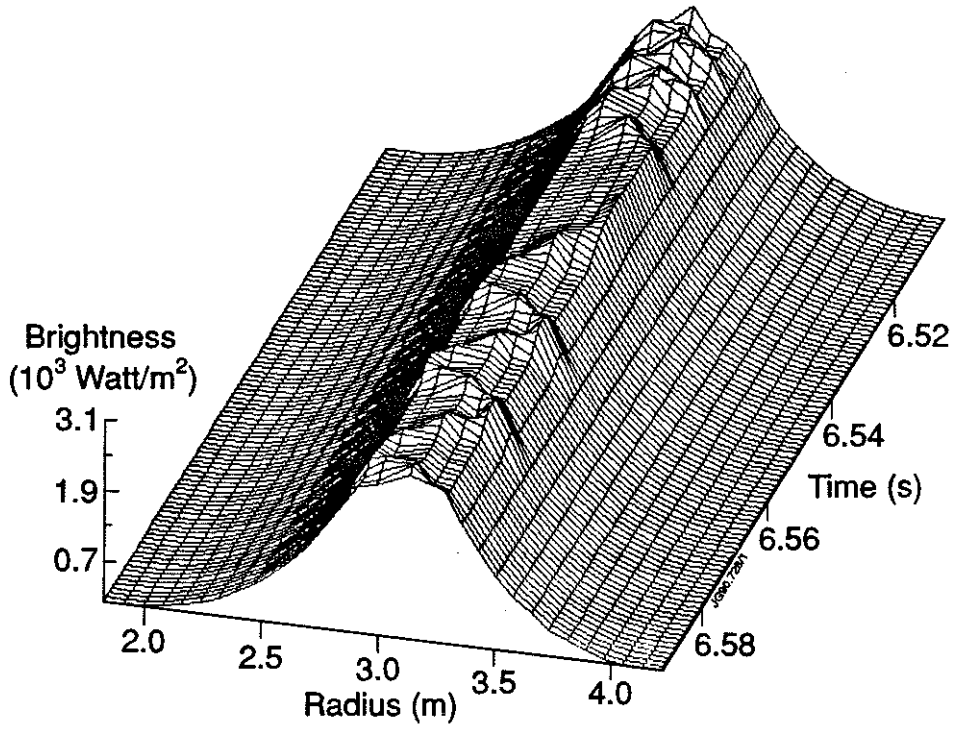

Fig. 9 A snake observed in an ohmic discharge with no pellet injections.

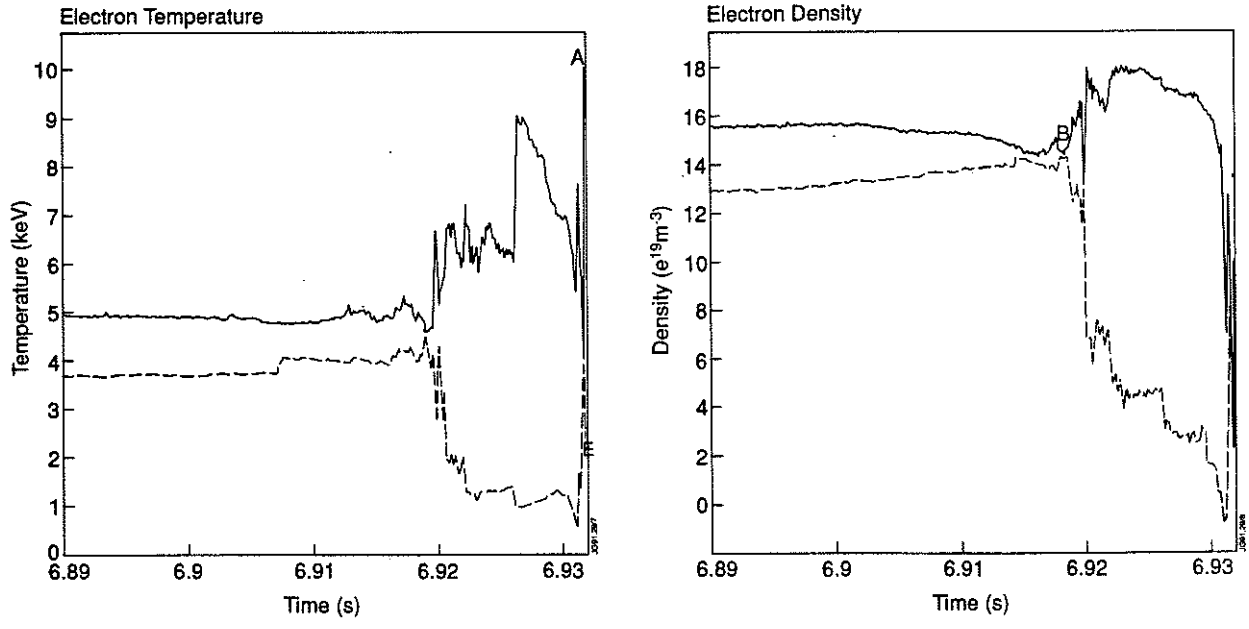

Fig. 10 Development of the plasma density and temperature preceeding a disruption. The solid curve corresponds to the plasma centre and the dashed curve is at r/a ~ 0.15. Pronounced peaking occurs at late times.

APPENDIX 1.

THE JET TEAM

JET Joint Undertaking, Abingdon, Oxon, OX14 3EA, U.K.

J.M.Adams[1], F.Alladio[4], H.Altmann, R.J.Anderson, G.Appruzzese, W.Bailey, B.Balet, D.V.Bartlett, L.R.Baylor[24], K.Behringer, A.C.Bell, P.Bertoldi, E.Bertolini, V.Bhatnagar, R.J.Bickerton, A.Boileau[3], T.Bonicelli, S.J.Booth, G.Bosia, M.Botman, D.Boyd[31], H.Brelen, H.Brinkschulte, M.Brusati, T.Budd, M.Bures, T.Businaro[4], H.Buttgereit, D.Cacaut, C.Caldwell-Nichols, D.J.Campbell, P.Card, J.Carwardine, G.Celentano, P.Chabert[27], C.D.Challis, A.Cheetham, J.Christiansen, C.Christodoulopoulos, P.Chuilon, R.Claesen, S.Clement[30], J.P.Coad, P.Colestock[6], S.Conroy[13], M.Cooke, S.Cooper, J.G.Cordey, W.Core, S.Corti, A.E.Costley, G.Cottrell, M.Cox[7], P.Cripwell[13], F.Crisanti[4], D.Cross, H.de Blank[16], J.de Haas[16], L.de Kock, E.Deksnis, G.B.Denne, G.Deschamps, G.Devillars, K.J.Dietz, J.Dobbing, S.E.Dorling, P.G.Doyle, D.F.Düchs, H.Duquenoy, A.Edwards, J.Ehrenberg[14], T.Elevant[12], W.Engelhardt, S.K.Erents[7], L.G.Eriksonn[5], M.Evrard[2], H.Falter, D.Flory, M.Forrest[7], C.Froger, K.Fullard, M.Gadeberg[11], A.Galetsas, R.Galvao[8], A.Gibson, R.D.Gill, A.Gondhalekar, C.Gordon, G.Gorini, C.Gormezano, N.A.Gottardi, C.Gowers, B.J.Green, F.S.Griph, M.Gryzinski[26], R.Haange, G.Hammett[6], W.Han[9], C.J.Hancock, P.J.Harbour, N.C.Hawkes[7], P.Haynes[7], T.Hellsten, J.L.Hemmerich, R.Hemsworth, R.F.Herzog, K.Hirsch[14], J.Hoekzema, W.A.Houlberg[24], J.How, M.Huart, A.Hubbard, T.P.Hughes[32], M.Hugon, M.Huguet, J.Jacquinot, O.N.Jarvis, T.C.Jernigan[24], E.Joffrin, E.M.Jones, L.P.D.F.Jones, T.T.C.Jones, J.Källne, A.Kaye, B.E.Keen, M.Keilhacker, G.J.Kelly, A.Khare[15], S.Knowlton, A.Konstantellos, M.Kovanen[21], P.Kupschus, P.Lallia, J.R.Last, L.Lauro-Taroni, M.Laux[33], K.Lawson[7], E.Lazzaro, M.Lennholm, X.Litaudon, P.Lomas, M.Lorentz-Gottardi[2], C.Lowry, G.Magyar, D.Maisonnier, M.Malacarne, V.Marchese, P.Massmann, L.McCarthy[28], G.McCracken[7], P.Mendonca, P.Meriguet, P.Micozzi[4], S.F.Mills, P.Millward, S.L.Milora[24], A.Moissonnier, P.L.Mondino, D.Moreau[17], P.Morgan, H.Morsi[14], G.Murphy, M.F.Nave, M.Newman, L.Nickesson, P.Nielsen, P.Noll, W.Obert, D.O'Brien, J.O'Rourke, M.G.Pacco-Düchs, M.Pain, S.Papastergiou, D.Pasini[20], M.Paume[27], N.Peacock[7], D.Pearson[13], F.Pegoraro, M.Pick, S.Pitcher[7], J.Plancoulaine, J-P.Poffé, F.Porcelli, R.Prentice, T.Raimondi, J.Ramette[17], J.M.Rax[27], C.Raymond, P-H.Rebut, J.Removille, F.Rimini, D.Robinson[7], A.Rolfe, R.T.Ross, L.Rossi, G.Rupprecht[14], R.Rushton, P.Rutter, H.C.Sack, G.Sadler, N.Salmon[13], H.Salzmann[14], A.Santagiustina, D.Schissel[25], P.H.Schild, M.Schmid, G.Schmidt[6], R.L.Shaw, A.Sibley, R.Simonini, J.Sips[16], P.Smeulders, J.Snipes, S.Sommers, L.Sonnerup, K.Sonnenberg, M.Stamp, P.Stangeby[19], D.Start, C.A.Steed, D.Stork, P.E.Stott, T.E.Stringer, D.Stubberfield, T.Sugie[18], D.Summers, H.Summers[20], J.Taboda-Duarte[22], J.Tagle[30], H.Tamnen, A.Tanga, A.Taroni, C.Tebaldi[23], A.Tesini, P.R.Thomas, E.Thompson, K.Thomsen[11], P.Trevalion, M.Tschudin, B.Tubbing, K.Uchino[29], E.Usselmann, H.van der Beken, M.von Hellermann, T.Wade, C.Walker, B.A.Wallander, M.Walravens, K.Walter, D.Ward, M.L.Watkins, J.Wesson, D.H.Wheeler, J.Wilks, U.Willen[12], D.Wilson, T.Winkel, C.Woodward, M.Wykes, I.D.Young, L.Zannelli, M.Zarnstorff[6], D.Zasche[14], J.W.Zwart.

PERMANENT ADDRESS

1. UKAEA, Harwell, Oxon. UK.
2. EUR-EB Association, LPP-ERM/KMS, B-1040 Brussels, Belgium.
3. Institute National des Récherches Scientifique, Quebec, Canada.
4. ENEA-CENTRO Di Frascati, I-00044 Frascati, Roma, Italy.
5. Chalmers University of Technology, Göteborg, Sweden.
6. Princeton Plasma Physics Laboratory, New Jersey, USA.
7. UKAEA Culham Laboratory, Abingdon, Oxon. UK.
8. Plasma Physics Laboratory, Space Research Institute, Sao José dos Campos, Brazil.
9. Institute of Mathematics, University of Oxford, UK.
10. CRPP/EPFL, 21 Avenue des Bains, CH-1007 Lausanne, Switzerland.
11. Risø National Laboratory, DK-4000 Roskilde, Denmark.
12. Swedish Energy Research Commission, S-10072 Stockholm, Sweden.
13. Imperial College of Science and Technology, University of London, UK.
14. Max Planck Institut für Plasmaphysik, D-8046 Garching bei München, FRG.
15. Institute for Plasma Research, Gandhinagar Bhat Gujat, India.
16. FOM Instituut voor Plasmafysica, 3430 Be Nieuwegein, The Netherlands.
17. Commissiariat à L'Energie Atomique, F-92260 Fontenay-aux-Roses, France.
18. JAERI, Tokai Research Establishment, Tokai-Mura, Naka-Gun, Japan.
19. Institute for Aerospace Studies, University of Toronto, Downsview, Ontario, Canada.
20. University of Strathclyde, Glasgow, G4 ONG, U.K.
21. Nuclear Engineering Laboratory, Lapeenranta University, Finland.
22. JNICT, Lisboa, Portugal.
23. Department of Mathematics, Univeristy of Bologna, Italy.
24. Oak Ridge National Laboratory, Oak Ridge, Tenn., USA.
25. G.A. Technologies, San Diego, California, USA.
26. Institute for Nuclear Studies, Swierk, Poland.
27. Commissiariat à l'Energie Atomique, Cadarache, France.
28. School of Physical Sciences, Flinders University of South Australia, South Australia SO42.
29. Kyushi University, Kasagu Fukuoka, Japan.
30. Centro de Investigaciones Energeticas Medioambientales y Techalogicas, Spain.
31. University of Maryland, College Park, Maryland, USA.
32. University of Essex, Colchester, UK.
33. Akademie de Wissenschaften, Berlin, DDR.

CR 88.49.1A